RESEARCH ARTICLE

Structural Evolution and Enhanced Energy Density, Ferroelectric Property Investigation in Gd Substituted NBT – BT Lead Free Ferroelectric Ceramics

K.S.K.R. Chandra Sekhar[1], M.L.V. Mahesh[2], Y. Rama Krishna[1], K. Chandra Mouli[1], R. Ramchandra Kiran[3], Patri Tirupathi[3,*]

[1]Department of Engineering Physics, A.U. College of Engineering (A), Andhra University, Visakhapatnam, Andhra Pradesh 530003, India
[2]Defence Metallurgical Research Laboratory, Hyderabad 500058, India
[3]Rajiv Gandhi University of Knowledge Technologies, IIIT – Idupulapaya, Kadapa, Andhra Pradesh, India

*Corresponding author: E-mail: p.thirupathi@rguktrkv.ac.in; Tel.: 7674862873

DOI: 10.5185/amlett.2021.041622

Gd substituted 0.94($Na_{0.5}Bi_{0.5-x}Gd_xTiO_3$) – 0.06 $BaTiO_3$ (x = 0.00, 0.01, 0.02 and 0.03) lead free ferroelectric ceramics were synthesized by a conventional solid-state synthesis. Room temperature XRD reveals the formation of perovskite structure without secondary impurity peaks. Rietveld refinement pattern confirms the coexistence of dual phase i.e., major monoclinic (Cc) and minor tetragonal (P4mm). More tetragonality and slim ferroelectric properties were noted with increasing Gd content in NBT-BT solid solutions. A collective Gd substitution stimulates the transition of PE loop shape from square to slim with slanted leads to suit for high energy density storage applications. The optimum energy storage properties can be achieved for x = 0.03 ceramic showed a recoverable energy density 1.59 J/cm³ and a remarkably best energy efficiency of 67% under 65 kV/cm at room temperature.

Introduction

Awareness in lead-free piezo electrics and ferroelectrics has grown owing to concerns around the toxicity of lead and resultant environmental legislation implemented in several countries [**1-3**]. Sodium bismuth titanate, $Na_{0.5}Bi_{0.5}TiO_3$ (NBT), and its solid solutions with other perovskites are some of the most heavily studied lead-free ferroelectric ceramic materials [**4**]. NBT, discovered by Smolenskii *et. al.* [**5**] in 1961, relaxor ferroelectric material exhibits a frequency dependence with respect to temperature of maximum permittivity (T_m). NBT exhibit large remnant polarisation (P_r) = 38 μC/cm², Coercive field (E_c) = 73 kV/cm and piezoelectric coefficient (d_{33}) = 70 pC/N [**6**]. The ground state structure of NBT is still in controversy even six decades after its discovery [**7**]. Recent high-resolution diffraction studies of NBT have suggested monoclinic average structure (Cc) [**8-10**] and also coexistence of monoclinic and rhombohedral phases [**11,12**]. A drawback of NBT ceramics for practical, e.g. piezoelectric, applications arise from the difficulty to polarize them because of their large coercive fields together with their high conductivity [**13**].

Among the solid solutions of NBT, $BaTiO_3$ (BT) modified NBT system, (1-x) $Na_{0.5}Bi_{0.5}TiO_3$ – (x) $BaTiO_3$ has gained most importance. (1-x) NBT – (x)BT emerges as promising candidate among the lead-free piezoelectric systems with a Rhombohedral (R) and Tetragonal (T) phase combination that termed as Morphotropic Phase boundary (MPB) at x = 0.06, where it has large piezoelectric response and electric field induced strain behaviour [**14-16**]. Similar to NBT, there is lack of unanimity with regard to the structure – ferroelectric property correlations of NBT [**17**]. In recent times, lead free ceramics grab much attention because of its energy storage ability. Few literature surveys propounded that, anti – ferroelectric (AFE) materials have a high energy storage density and better dielectric properties rather than normal ferroelectric (FE) materials. Ferroelectrics often have larger saturated polarization and modest electric-field endurance, but their larger remnant polarization (P_r) leads to a smaller energy-storage density and lower efficiency. Relaxor ferroelectrics and antiferroelectric are more likely to be used for high energy storage rather than ferroelectrics because of their larger saturated polarization, smaller remnant polarization and moderate breakdown field [**18**]. To improve the electric properties and to enhance the energystorage density of NBT - BT ceramics, the effects of A – Site, B – Site or simultaneous A and B sites substitution with rare earth (RE) elements were extensively studied. It has been reported that the partial substitution of some rare-earth ions such as Ho^{3+}/Dy^{3+}/$Nd^{3+}$and Er^{3+} for Bi^{3+} in NBT based lead free ceramics can develop new multifunctional materials with excellent structural, dielectric, ferroelectric, piezoelectric, photoluminescent and other optical properties [**19-22**]. As the Gadolinium (Gd^{3+}), is a rare earth ion, wellknown for its improving character of pyroelectric properties [**23**]. Moreover, Gd^{3+} insertion in NBT increases the dielectric, ferroelectric properties and also exhibits antiferroelectric pinched P – E hysteresis loops at raised temperatures for

high energy storage density applications [**24**]. Gd^{3+} ion substitution initiates a point charge defect by means of oxygen vacancies along with producing the formation of unit cell distortion [**25**].

In the present work, influence of Gd^{3+} substitution in NBT – BT on structural, microstructural, ferroelectric and energy storage density properties of NBT-BT have been reported.

Experimental

Lead free Gd substituted 0.94 ($Na_{0.5}Bi_{0.5-x}Gd_xTiO_3$) – 0.06($BaTiO_3$) (x = 0.01, 0.02 and 0.03) (Abbreviated as NBTBT, $NBTBTGd_1$, $NBTBTGd_2$, $NBTBTGd_3$ for x = 0.00, 0.01, 0.02 & 0.03 respectively) diffuse ferroelectric ceramics has been prepared by conventional solid-state reaction method. High purity A.R. Grade Na_2CO_3, Bi_2O_3, Gd_2O_3, $BaCO_3$ and TiO_2 (≥99.99%, Sigma Aldrich, USA) were taken as starting precursors to prepare the ceramics. The stoichiometric amounts of oxides and carbonates were thoroughly mixed with 2 – Propanol in agate mortar for 6 – 8 hours, and then calcined at 800°C for 3 hours. The lump is again finely grinded for 1 – 2 hours and a suitable amount (5 wt%) of Poly Vinyl Alcohol (PVA) is used as binder. The grinded powders were pressed into disks of 10 mm in diameter and 1 – 2 mm in thickness by applying a uniaxial pressure of 4 MPa. The pellets were sintered at 1130°C for 3 hours in air. The structural phase purity of the samples was monitored by X – ray diffraction (XRD) technique by using an (PANlytical X'Pert PRO with CuK_α, λ = 1.5406Å) in range of 20° ≤ 2θ ≤ 80° with scan rate 0.0167°/sec. The surface morphology was studied by scanning electron microscope (SEM, JSM-6390, Japan). Raman spectra at room temperature were recorded with a Renishaw in Via Reflex Raman Microscope using monochromatic radiation emitted by an Ar-Ion laser source of wavelength 470 nm. The room temperature Polarisation (P) V/s Electric field (E) measurements were carried out by using Aixacct TF 2000 analyser with loop frequency 1Hz on the silver - electrode samples after DC poling in Silicone oil bath.

Results and discussion

Structural phase transitions with Rietveld refinement technique

The XRD pattern of all sintered Gd substituted NBT-BT solid solutions at room temperature are shown in **Fig. 1**. The observed XRD patterns exhibit a pure perovskite type structure without any secondary/impurity phases, implying that Ba^{2+} and Gd^{3+} ions have diffused into the NBT lattices to form a solid solution. With substitution of Gd at Bi-site, the peak (110) slightly shifts towards higher angle that indicated a lattice shrink as a consequence of decrease of crystallite size was shown in the range 32° to 33°. The Crystallite size was calculated using Debye – Scherrer formula;

$$D = \frac{0.89\,\lambda}{\beta_{1/2} Cos\,\theta} \quad (1)$$

where D is the crystallite size (μm), λ is the wavelength of $CuK\alpha$ radiation, $\beta_{1/2}$ is the full width at half maximum intensity of the characteristic (110) peak and θ is the angle of diffraction in radians. The crystallite size is found to decrease with increasing of Gd concentration. The noted values for crystallite size were 0.021 μm, 0.0377 μm, 0.0348 μm and 0.0332 μm for x = 0.00, 0.01, 0.02 and 0.03 respectively.

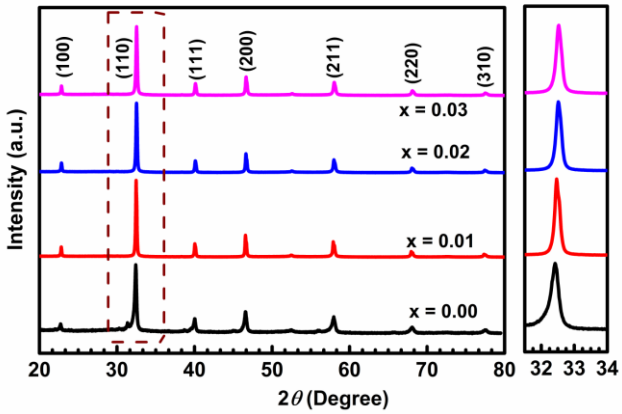

Fig. 1. X-ray diffraction patterns of NBT – BT ceramics with substitution of Gd (0.00 ≤ x ≤ 0.03).

In perovskite ceramics, the crystallite size effects always depend on average ionic radii either A –site or B-site ions in ABO_3 perovskite. Here the main factor to determine the lattice distortion and crystallite size is in terms tolerance factor 't' can be defined as

$$t = \frac{R_A + R_O}{\sqrt{2}\,(R_B + R_O)} \quad (2)$$

where R_A, R_B and R_O are the effective ionic radii of the A-site cation, B-site cation and oxygen in ABO_3 perovskite, respectively. Generally, ionic radii of B-site and oxygen ion remain unaltered. On the other hand, the A-site element Bi (1.17 Å) ion substituted by Gd^{3+} (1.053 Å) ion, respectively, with doping of Gd^{3+} ion, the average ionic radii in A-site decreases, hence tolerance 't' values decrease. Henceforth, a slight decrease in crystallite size was noticed in Gd substituted NBT-BT ceramics.

The exact phase impact of each solid solution can be estimated quantitatively with help of Rietveld refinement method. The recent literature provokes an ambiguity on room temperature crystal structure of NBT i.e., between monoclinic Cc [**11**] to rhombohedral R3c phase [**12**]. The electrical poling of sintered NBT ceramics stabilize the rhombohedral with R3c space group, wherever at strengthening the argument of stability of Cc at room temperature without poled samples. Further it is known that $BaTiO_3$ has tetragonal crystal structure with P4mm phase at room temperature. In contrast, the recent High resolution XRD and Neutron diffraction study on NBT-BT solid solution represents the existence of Cc, rather than R3c phase. Keeping this point in view, scrutiny on the several existence dual phase models i.e., R3c+P4mm, Cc+Pbnm, R3c+Pbnm and Cc + P4mm etc. in Gd

modified NBT-BT solid solutions. During refinement, the background was modelled with n-polynomial function, whereas atomic positions, lattice parameters, isothermal parameters were also refined. Finally, Cc+P4mm dual phase model gave the satisfactory fit that confirms the structural coexistence near the morphotropic phase boundary. The matching between the experimental and calculated XRD pattern is relatively good based on the consideration of goodness of fitting parameters χ^2, R_p and R_{wp} shown in **Table 1**. **Fig. 2(a-d)** show the Rietveld refined XRD pattern of Gd substituted NBT-BT solid solutions. Further with the increase of Gd content (x) in NBT-BT from 0.01 to 0.03 the tetragonality (%) increases. The refined lattice constants, atomic positions, and refinement values are tabulated in **Table 1**.

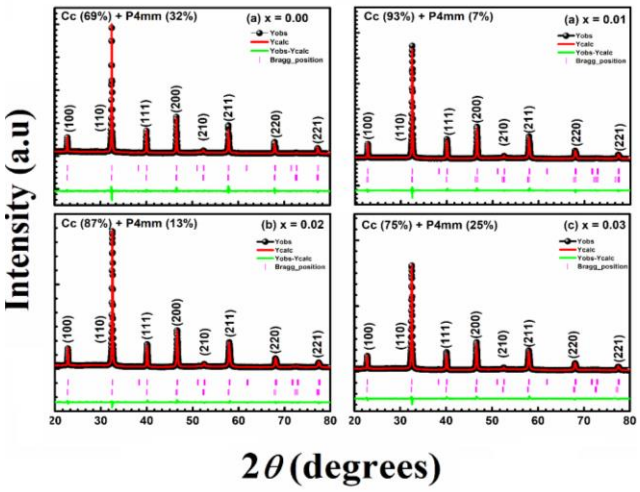

Fig. 2. (a-d) Rietveld refinement studies of Gd substituted NBT – BT ceramics ($0.00 \leq x \leq 0.03$).

Raman spectroscopic studies

To confirm phase purity and structural evolution in micro level, vibrational mode analysis by Raman spectroscopic study has been carried out for Gd modified NBT-BT solid solutions. **Fig. 3(a) & Fig. 3(b)** depicts the Raman Spectroscopic patterns for Gd substituted NBT – BT ($0.00 \leq x \leq 0.03$) and deconvoluted Raman spectrum for undoped NBT – BT ceramics respectively, that reveals the structural transformation and distortions in solid solutions. The observed Raman bands are relatively broad in nature that might be due to the cationic disorder on the A and B–sites in ABO_3 perovskites [**26**]. Here we noted six vibrational modes in visible spectrum near at 125, 280, 533, 582, 757 and 861 cm^{-1} as indicated in the **Fig. 3(a),** which are in good agreement with previous literature **[27-29]**. The bands around below 200 cm^{-1} regime are attributed to A-site cation in perovskites (ABO_3) such as Bi-O/ Na-O bonds. Above 200 cm^{-1} regime, the noted bands are attributed to B-site cation in perovskites. In addition, we noted band at 280 cm^{-1} is attributed to Ti – O bonds that arise due to the torsional bending of TiO_6 octahedra [**30**]. The low frequency bands at 125 and 280 cm^{-1} are very sensitive to a little structural transitions and display mode softening during phase transitions [**31,32**]. The high frequencies bands around 533 and 582 cm^{-1} are also well known for NBT – based ceramics that are related to vibrations caused by TiO_6 Octahedron [**30**]. In recent literature, the bands observed at high frequencies near at (757 and 861 cm^{-1}) are ascribed to diffusion of oxygen vacancies or monotonic increase in its intensity to vacancy concentration. Most of these bands noted in pure and NBT-BT solid solutions indicate the Bismuth volatility during sintering [**33**]. The presence of such an unexpected high frequency band is observed in some rare earth doped perovskites by Mineshige *et. al.* [**30,31**]. Furthermore, overlapping of high frequency bands into single broad peak in Gd substituted NBT-BT ceramics are noted. This implies that the degree of distortion for more stable in tetragonality with increasing Gd dopant. It concludes that the level of substituent at Bi-site by rare earth elements induces structural distortion which plays a key role in enriching the electrical and ferroelectric properties [**34**].

Table 1. Structural refined parameters of Monoclinic (Cc) along with Tetragonal (P4mm) phases for Gd substituted NBT – BT ceramics.

Phase and atoms	Atomic Positions			Lattice parameters (a,b,c) (Å), R_p, R_{wp} and χ^2 values with Concentration of Gd (x) mol %			
	x	y	z	x = 0.00	x = 0.01	x = 0.02	x = 0.03
Cc							
Na/Bi/Ba/Gd	0.0000	0.2500	0.0000	a = 9.5543	a = 9.5359	a = 9.5467	a = 9.5488
Ti	0.2540	0.2421	0.7466	b = 5.5150	b = 5.5138	b = 5.4992	b = 5.5012
O_1	-0.0069	0.2764	0.5471	c = 5.5178	c = 5.5101	c = 5.5100	c = 5.5085
O_2	0.2932	0.5349	0.1116	α = γ = 90°	α = γ = 90°	α = γ = 90°	α = γ = 90°
O_3	0.2922	-0.0148	0.0905	β = 125.2930°	β = 125.2116°	β = 125.3072°	β = 125.3070°
P4mm							
Na/Bi/Ba/Gd	0.0000	0.0000	0.0000	a=b= 3.9023	a=b= 3.8961	a=b= 3.8997	a=b= 3.9038
Ti	0.5000	0.5000	0.5465	c = 3.9108	c = 3.9306	c = 3.9196	c = 3.9125
O_1	0.5000	0.5000	0.2323	α= β=γ = 90°	α= β=γ = 90°	α= β=γ = 90°	α= β=γ = 90°
O_2	0.5000	0.0000	0.5150				
				Cc (69%) + P4mm (32%)	Cc (93%) + P4mm (7%)	Cc (87%) + P4mm (13%)	Cc (75%) + P4mm (25%)
				R_p = 19.9	R_p = 10.2	R_p = 7.97	R_p = 10.1
				R_{wp} = 13.9	R_{wp} = 8.81	R_{wp} = 7.82	R_{wp} = 9.31
				χ^2 = 3.213	χ^2 = 4.736	χ^2 = 4.557	χ^2 = 7.146

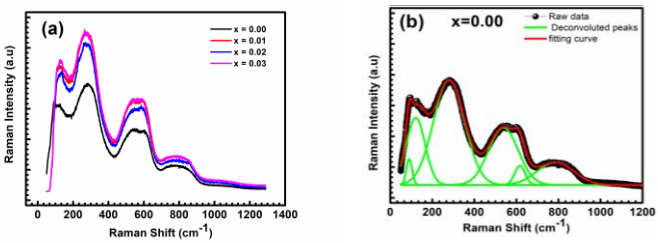

Fig. 3. (a) Raman Spectroscopic patterns for Gd substituted NBT – BT ($0.00 \leq x \leq 0.03$) and (b) Deconvoluted Raman spectrum for undoped NBT – BT (x=0.00).

Surface morphology studies

Fig. 4(a-d) shows the SEM micrographs of Gd doped NBT-BT ceramics with x = 0.00, 0.01, 0.02 and 0.03 compositions respectively. The microstructure appears homogeneous with dense and pore – free structure, giving a high relative density (above 95%). The slight reduction in grain size was noted with substitution of Gd, indicate the clear inhibition of Gd^{3+} ions in host NBTBT lattice. The average calculated grain size of ceramics was 0.85μm, 0.648μm, 0.511μm and 0.495μm for x = 0.00, 0.01, 0.02 and 0.03 respectively. **Fig. 4(e-h)** indicating the average grain size (μm) histograms for x = 0.00, 0.01, 0.02 and 0.03 respectively.

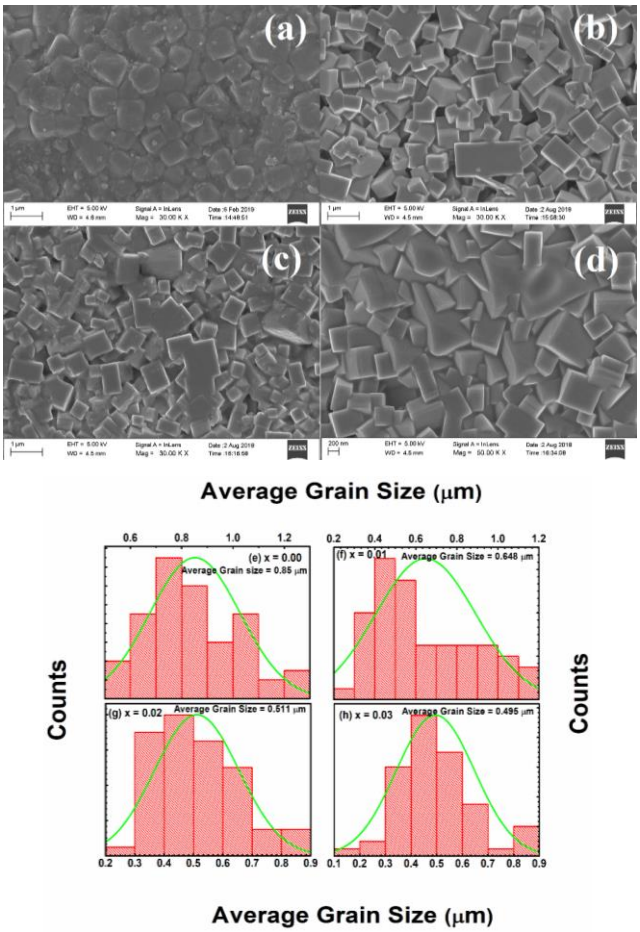

Fig. 4. (a-d) SEM micrographs for the Gd substituted NBT – BT ($0.00 \leq x \leq 0.03$) and (e-h) shows the histograms depict their respective average grain size (μm).

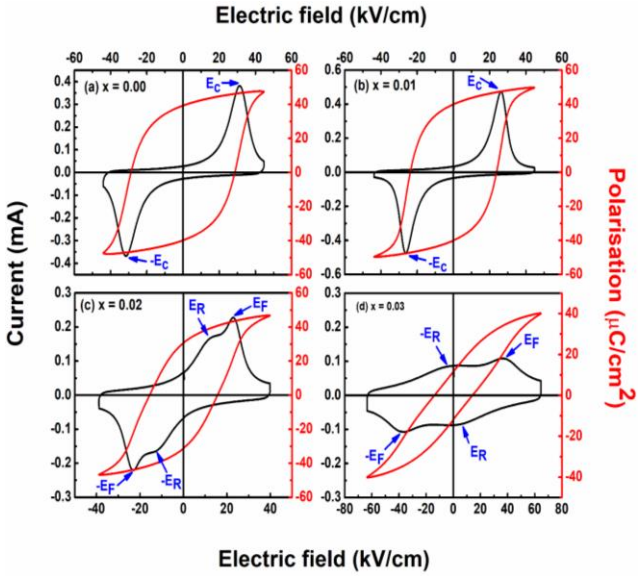

Fig. 5. (a-d) Polarisation (P) – Current (I) – Electric field (E) curves for the Gd substituted NBT – BT ($0.00 \leq x \leq 0.03$) at room temperature.

Room temperature ferroelectric studies

Fig. 5(a-d) shows the P-E hysteresis loops and I-E curves of NBT-BT-Gd (*x*=0.00, 0.01, 0.02 &0.03) at 1 Hz loop frequency. The essential sample parameters for P – E measurement such as thickness (mm) and electrode area are given below.

Sample	Thickness (mm)	Electrode area (mm^2)
x = 0.00	0.91	52.84
x = 0.01	0.75	49.86
x = 0.02	0.64	47.15
x = 0.03	0.73	48.99

The parent ceramics NBT-BT exhibited constricted square loop with long range FE order associated, was a characteristic feature of hard ferroelectrics. The substitution of rare earth ion Gd^{3+} in NBT-BT ceramics, leads to more tetragonality with is antiferroelectric character. Compared to monoclinic Cc (rhombohedral R3c) phase more in hard ferroelectric character that were noticed in XRD analysis, where Gd substitution increases tetragonality. Henceforth, we noticed a slim asymmetric ferroelectric loop in Gd^{3+} substitution NBT-BT ceramics. On the other hand, in lanthanides 4f electrons have more insulating property and screening effect, which reduce the oxygen vacancies due to effective nuclear charge (Z_{eff}) in Gd in NBT-BT ceramics leads to slim ferroelectric property. With increment of Gd the coercive field reduces greatly from 32kV/cm to 23kV/cm compared with pure NBT-BT. Further, the polarization loops become slim and slanted with obvious decrement in P_r from 41 to 12 μC/cm^2 values noted with increment of Gd substitution from x = 0.00 to 0.03. The improvement of ferroelectric property such as slight decrease in P_r and reduction in E_c with Gd in NBT-BT will facilitate the mobility of domain

wall. It can be elucidated that the long-range dipolar interaction is associated with dislocation by the dopant ions. Subsequently local isolated polar nano regions (PNRs) are formed from the composition fluctuation and charge difference [**33,35**]. The substitution of Gd in NBT – BT triggers the reduction of coercivity which suited for easy switching of NBT based devices. The low P_r, together with relatively large P_s at field strength of 40kV/cm favours the improvement of energy storage density for Gd doped NBT-BT ceramics. The compositional variation of current can be illustrated in P-I-E curves of **Fig. 5(a)–(d)**. Two typical peaks exist on the I – E curve in **Fig. 5(a–d)** are corresponding to domain switching and changing electric field with current maxima at coercive field is a sign of ferroelectricity [**35**].

By the increase in Gd content from x = 0.02 to x = 0.03, the P-E loops become slim and slanted. The ceramic with x = 0.02 exhibits four current peaks on the I-E curve, which are denoted as ± E_R and ± E_F in the different quadrants. It has been suggested that the emergence of the peaks around ± E_R and ± E_F are related to the coexistence of ergodic and non-ergodic phases [**36**]. As the Gd^{3+} content further increases to x = 0.03, the peaks on the I-E curves become gradually blurred/vanished, which are typical character for relaxor ferroelectrics [**37,38**].

Recoverable energy storage density study

The recoverable energy density (W_{rec}) and energy loss (W_{loss}) can be calculated by integrating the effective area between the polarization axis and the discharging curve of the polarization vs electric field (P-E) hysteresis loops using Equations (3) and (4) [**37**].

$$W_{rec} = \int_{P_r}^{P_{max}} Edp \quad (3)$$

$$W_{loss} = \int_{0}^{P_{max}} Edp \quad (4)$$

here P_{max} is the highest polarisation (saturation polarisation (P_s)) and E is the electric field. Consequent calculation of the energy – storage efficiency (η) can be expressed as Equation (5):

$$\eta = \frac{W_{rec}}{W_{rec}+W_{loss}} \times 100\% \quad (5)$$

The influence of Gd substitution on the recoverable energy storage density (W_{rec}) is depicted in **Fig. 6(a)**. It can be observed that, with the increase of Gd substitution W_{rec} increases from 0.39 J/cm^3 to 1.59 J/cm^3 and while W_{loss} decreases from 1.27 J/cm^3 to 0.78 J/cm^3, was shown in inset **Fig. 6(a)**. The calculated energy storage efficiency (η) values are 23, 27, 41 and 67 % for undoped NBTBT, NBTBT-Gd (0.01) NBTBT-Gd (0.02), NBTBT-Gd (0.03) respectively. The energy storage properties of high dopant substituted (i.e., 0.94 ($Na_{0.5}Bi_{0.47}Gd_{0.03}TiO_3$) – 0.06 $BaTiO_3$, simply indicated by x = 0.03) is a best suitable candidate for energy storage applications. The observed energy storage density values shown that Gd doped NBT-BT ceramics can be favourable candidates for energy storage applications at room temperature. Furthermore, we focussed on field dependent energy storage properties for x = 0.03 ceramic, however **Fig. 6(b)** presents the P – E loops with different field of the ceramic x = 0.03. It can be observed from **Fig. 6(b)** that the values of remnant polarization (P_r) have a negligible fluctuation and the maximum polarization (P_{max}) increases from 34 to 41 μC/cm^2. The observed values of maximum polarization (P_{max}) are 34.3, 36.9, 38.1, 39.9 and 40.93 μC/cm^2 for the applied field strengths 55, 60, 62, 65 and 67 kV/cm respectively. Furthermore, we observed that the shape of P-E loops has slightly changed that indicates stabilization and less dependence on the applied electric field. The room temperature energy storage activity for the x = 0.03 ceramic with increase electric field can be illustrated in **Fig. 6(c)**. There is an increase in the recoverable energy storage density from 0.47 to 1.59 J/cm^3 with an increase of electric field strength from 40 to 67 kV/cm field for the x = 0.03 ceramic. Inset **Fig. 6(c)** displays the recoverable energy storage (W_{rec}) region. This was indexed in green shaded region and the energy loss (W_{loss}) region was indexed in red shaded region to calculating the energy storage density and energy loss density with integrating area under the curves using the equations (3) and (4) respectively. (The energy storage efficiency (%) values are changed slightly with electric fields; a maximum storage efficiency is observed about 67% at maximum field that makes the ceramic x = 0.03 is suitable for energy storage applications.

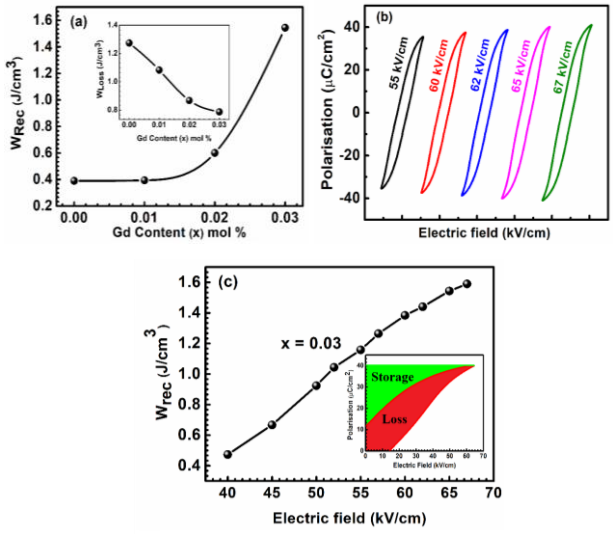

Fig. 6. (a). Variation of recoverable energy storage density (W_{Rec}) for Gd substituted NBT – BT ($0.00 \leq x \leq 0.03$) ceramics and energy loss density (W_{loss}) shown in inset. (b) Saturated P-E loops for x = 0.03 ceramic at different electric fields. (c) Electric field induced energy storage properties of x = 0.03 ceramic and representation of storage and loss regions in inset.

Conclusion

In summary, lead free Gd substituted 0.94 ($Na_{0.5}Bi_{0.5-x}Gd_xTiO_3$) – 0.06($BaTiO_3$) (x = 0.00, 0.01, 0.02 and 0.03) ceramics were successfully prepared by the conventional solid-state reaction method. Formation of pure perovskite phase with no impurity was confirmed by X-ray diffraction. The Coexistence of Monoclinic (Cc) and Tetragonal (P4mm) phases was approved by Rietveld refinement study. Tetragonality (%) was found to increase with the increase of Gd substitution in NBT – BT host lattices. In this study, the optimum energy-storage properties (W_{rec} of 1.59 J/cm^3, and η of 67%) can be achieved in in x = 0.03 ceramic which can be explained on the basis of room temperature energy storage studies. Therefore, these experimental results suggest that the ceramics obtain well energy storage properties, which can be primely used in energy storage applications.

Acknowledgments

The author KCS would like to acknowledge to Prof. V. Seshubai, UGC Networking resource centre (UGC – NRC), School of Physics, University of Hyderabad for providing X – ray diffraction studies and Dr. G. Vasanth Sathe, UGC – DAE – CSR, Indore Centre for providing Raman spectroscopic studies. The author TP would like to thank UGC - DAE, BARC - India, for (UDCSR/MUM/CD/CRSM-261/2017) the project funded under the collaborator research scheme.

Keywords

Lead free; sodium bismuth titanate ($Na_{0.5}Bi_{0.5}TiO_3$); energy storage density

Received: 2 September 2020
Revised: 14 November 2020
Accepted: 27 November 2020

References

1. Watson, J.; Castro, G.; *J. Mater. Sci. Mater. Electron.*, **2015**.
2. Bultitude, J.; McConnell, J.; Shearer, C.; *J. Mater. Sci. Mater. Electron.*, **2015**, *26*, 9236.
3. Zeb, A.; Milne, S. J.; *J. Mater. Sci. Mater. Electron.*, **2015**, *26*, 9243.
4. Rödel, J.; Jo, W.; Seifert, K. T. P.; Anton, E.M; Granzow, T.; Damjanovic, D.; *J. Am. Ceram. Soc.*, **2009**, *92*, 1153.
5. Smolenskii, G. A.; Isupov, A. I.; Agranovskaya, A.; Krainik, N. N.; *Sov. Phys. Solid State*, **1961**, 2651.
6. Jaffe, B.; *Piezoelectric Ceramics*, **2012**, *3*.
7. Smolenskiĭ, G. A.; Chupis, I. E.; *Sov. Phys. Uspekhi*, **1982**, *25*, 475.
8. Gorfman, S.; Thomas, P. A.; *J. Appl. Crystallogr*, **2010**.
9. Aksel, E.; Forrester, J. S.; Jones, J. L.; Thomas, P. A.; Page, K.; Suchomel, M. R. *Appl. Phys. Lett.*, **2011**, *98*, 152901.
10. Aksel, E.; Forrester, J. S.; Kowalski, B.; Jones, J. L.; Thomas, P. A.; *Appl. Phys. Lett.*, **2011**.
11. Rao, B. N.; Ranjan, R.; *Phys. Rev. B*, **2012**, *86*, 134103.
12. Rao, B. N.; Fitch, A. N.; Ranjan, R.; *Phys. Rev. B*, **2013**, *87*, 60102.
13. Chu, B. J.; Chen, D. R.; Li, G. R. Yin, Q. R.; *J. Eur. Ceram. Soc.*, **2002**.
14. Chiang, Y. M.; Farrey, G. W.; Soukhojak, A. N.; *Appl. Phys. Lett.*, **1998**.
15. Takenaka, T.; Maruyama, K.; Sakata, K.; *Jpn. J. Appl. Phys.*, **1991**, *30*, 2236.
16. Jo, W.; Daniels, J. E.; Jones, J. L.; Tan, X.; Thomas, P. A.; Damjanovic, D.; Rödel, J.; *J. Appl. Phys.*, **2011**.
17. Garg, R.; Narayana Rao, B.; Senyshyn, A.; Ranjan, R.; *J. Appl. Phys.*, **2013**, *114*, 1.
18. Hao, X.; *J. Adv. Dielectr.*, **2013**, *3*, 1330001.
19. Zhou, L.; Zou, X.; Tian, M.; Lei, F.; Zheng, Q.; Sun, T.; Lin, D.; *J. Mater. Sci. Mater. Electron.*, **2015**, *26*, 6979.
20. Fu, P.; Xu, Z.; Chu, R.; Li, W.; Xie, Q.; Zhang, Y.; Chen, Q.; *J. Alloys Compd.*, **2010**, *508*, 546.
21. Lau, C. M.; Xu, X. W.; Kwok, K. W.; *Appl. Surf. Sci.*, **2015**, *336*, 314.
22. Zannen, M.; Lahmar, A.; Dietze, M.; Khemakhem, H.; Kabadou, A.; Es-Souni, M.; *Mater. Chem. Phys.*, **2012**, *134*, 829.
23. Sharma, H. D.; Tripathi, A. K.; Chariar, V.; Goel, T. C.; Pillai, P. K. C.; *Mater. Sci. Eng. B.*, **1994**, *25*, 29.
24. Zannen, M.; Lahmar, A.; Khemakhem, H.; El Marssi, M.; *Solid State Commun.*, **2016**, *245*, 1.
25. Santos, I. A.; Spınola, D. U.; Garcia, D.; Eiras, J. A.; *J. Appl. Phys.* **2002**, *92*, 3251.
26. Zhang, M.S.; Scott, J. F.; Zvirgzds, J. A.; *Ferroelectr. Lett. Sect.*, **1986**, *6*, 147.
27. Kreisel, J.; Glazer, A. M.; Jones, G.; Thomas, P. A.; Abello, L.; Lucazeau, G.; *J. Phys. Condens. Matter*, **2000**, *12*, 3267.
28. Kreisel, J.; Glazer, A. M.; Bouvier, P.; Lucazeau, G.; *Phys. Rev. B*, **2001**, *63*, 174106.
29. Selvamani, R.; Singh, G.; Sathe, V.; Tiwari, V. S.; Gupta, P. K.; *J. Phys. Condens. Matter*, **2011**, *23*, 55901.
30. Mineshige, A.; Okada, S.; Kobune, M.; Yazawa, T.; *Solid State Ionics*, **2006**, *177*, 2443.
31. Mineshige, A.; Okada, S.; Sakai, K.; Kobune, M.; Fujii, S.; Matsumoto, H.; Shimura, T.; Iwahara, H.; Ogumi, Z.; *Solid State Ionics*, **2003**, *162*, 41.
32. Cai, K.; Yan, X.; Deng, P.; Jin, L.; Bai, Y.; Zeng, F.; Guo, D.; *J. Mater.*, **2019**, *5*, 394.
33. Mayamae, J.; Sukkha, U.; Niemchareon, S.; Muanghlua, R.; Vittayakorn, N.; *Ferroelectrics*, **2016**, *490*, 23.
34. Huang, C.; Cai, K.; Wang, Y.; Bai, Y.; Guo, D.; *J. Mater. Chem. C*, **2018**, *6*, 1433.
35. Jin, L.; Li, F.; Zhang, S.; *J. Am. Ceram. Soc.*, **2014**, *97*, 1.
36. Li, F.; Zuo, R.; Zheng, D.; Li, L.; *J. Am. Ceram. Soc.*, **2015**, *98*, 811.
37. Yang, H.; Yan, F.; Lin, Y.; Wang, T.; *ACS Sustain. Chem. Eng.*, **2017**, *5*, 10215.
38. Xie, H.; Zhao, Y.; Xu, J.; Yang, L.; Zhou, C.; Zhang, H.; Zhang, X.; Qiu, W.; Wang, H.; *J. Alloys Compd.*, **2018**, *743*, 73.